Probing interlayer interaction via chiral phonons in layered honeycomb materials

Chen Chen,[1,*] Xiaolong Chen,[1,†] Bingchen Deng,[1] Kenji Watanabe,[2] Takashi Taniguchi,[3] Shengxi Huang,[4] and Fengnian Xia[1,‡]

[1]*Department of Electrical Engineering, Yale University, New Haven, Connecticut 06511, USA*
[2]*Research Center for Functional Materials, National Institute for Materials Science, 1-1 Namiki, Tsukuba 305-0044, Japan*
[3]*International Center for Materials Nanoarchitectonics, National Institute for Materials Science, 1-1 Namiki, Tsukuba 305-0044, Japan*
[4]*Department of Electrical Engineering, The Pennsylvania State University, University Park, University Park, Pennsylvania 16802, USA*

(Received 18 September 2020; accepted 16 December 2020; published 8 January 2021)

van der Waals (vdW) interaction plays a significant role in controlling the physical properties of layered materials. Typically, the vdW interlayer interaction can be calculated by density functional theory or experimentally characterized by quantum capacitance measurement. Here, we report the probing of the interlayer interaction in layered honeycomb materials via chiral phonons. Through helicity resolved Raman measurements, we observed a reduced chirality of the Raman *G* mode with increasing layer numbers. We introduced interlayer coupling terms into the traditional Raman *G* mode tensor to simulate the reduced phonon chirality in Raman spectra. Our Raman tensor calculation results agree with the experiments well, suggesting that the interlayer interaction can significantly influence the lattice vibration. Our demonstration provides a perspective for characterizing the interlayer interactions in vdW layered materials with honeycomb lattice structure.

DOI: 10.1103/PhysRevB.103.035405

I. INTRODUCTION

van der Waals (vdW) materials [1], assembling the layered materials bonded by the vdWs interlayer interaction, provided an emerging platform for investigating both the fundamental physics [2–5] and the device applications [6–9]. The interlayer interaction plays a critical role in controlling the physical properties of vdWs materials. For example, the band structure of the MoS_2 experiences a direct-to-indirect band-gap transition from monolayer MoS_2 to its multilayer counterpart due to the interlayer interaction [10,11]. Moreover, the band gap of black phosphorus (BP) can be tuned from around 2.0 eV in monolayer BP to 0.3 eV in its bulk limit [12,13], leading to photoluminescence emission from visible to midinfrared [14–16]. The strength of the interlayer interaction can be estimated by theoretical calculations utilizing the density functional theory [17], which has been demonstrated in many layered materials, e.g., graphene [18,19], transitional metal dichalcogenides [20,21], and hexagonal boron nitride (hBN) [22]. Experimentally the direct probe of interlayer interaction has been demonstrated through the low-frequency Raman spectroscopy [23–25]. Quantum capacitance measurements have also been applied to investigate the interlayer coupling strength, which is limited to few-layer graphene [26,27]. Therefore, it is desirable to develop other complementary approaches to experimentally characterize the strength of interlayer interactions.

In this paper, we report a strategy for probing the interlayer interaction via chiral phonons in layered honeycomb materials. The phonons in graphene exhibit distinct chiral properties due to its unique valley phonon scattering processes and the conservation of the pseudoangular momentum (PAM). Remarkably, the Raman *G* mode exhibits reduced phonon chirality with increasing layer number, evidenced by the decreasing polarization degree of the Raman signal in helicity resolved measurements. This observation suggests that the interlayer interaction plays a crucial role in the lattice vibration in layered honeycomb graphene lattice and therefore influences the phonon chirality. We introduced interlayer coupling terms to the fundamental Raman tensor to account for the effect of coupling. The calculated evolution of the phonon chirality versus the layer number based on the new Raman tensor agrees with the experimental results. The same layer number dependent phonon chirality was further observed in the Raman *G* mode of honeycomb hBN, further confirming the validity of our theory.

II. HELICITY RESOLVED RAMAN SPECTRUM IN GRAPHENE LAYERS

Graphene flakes with different layer numbers were directly deposited onto 90-nm SiO_2/Si substrate using the mechanical exfoliation method. Figure 1(a) shows the optical micrograph of graphene flakes used for Raman spectrum measurements. The layer numbers of the monolayer and few-layer graphene were first identified by the optical contrast [Fig. 1(b)] [28,29], which shows a monochromatically linear increase with layer numbers. The unpolarized Raman spectra further confirmed the layer numbers [Fig. 1(c)], which agreed well with previous Raman studies [30,31]. To investigate the Raman *D* mode arising from the defects which were absent in the pristine

*Corresponding author: chen.chen.cc2483@yale.edu
†Present address: Department of Electrical and Electronic Engineering, Southern University of Science and Technology, Shenzhen 518055, China.
‡Corresponding author: fengnian.xia@yale.edu

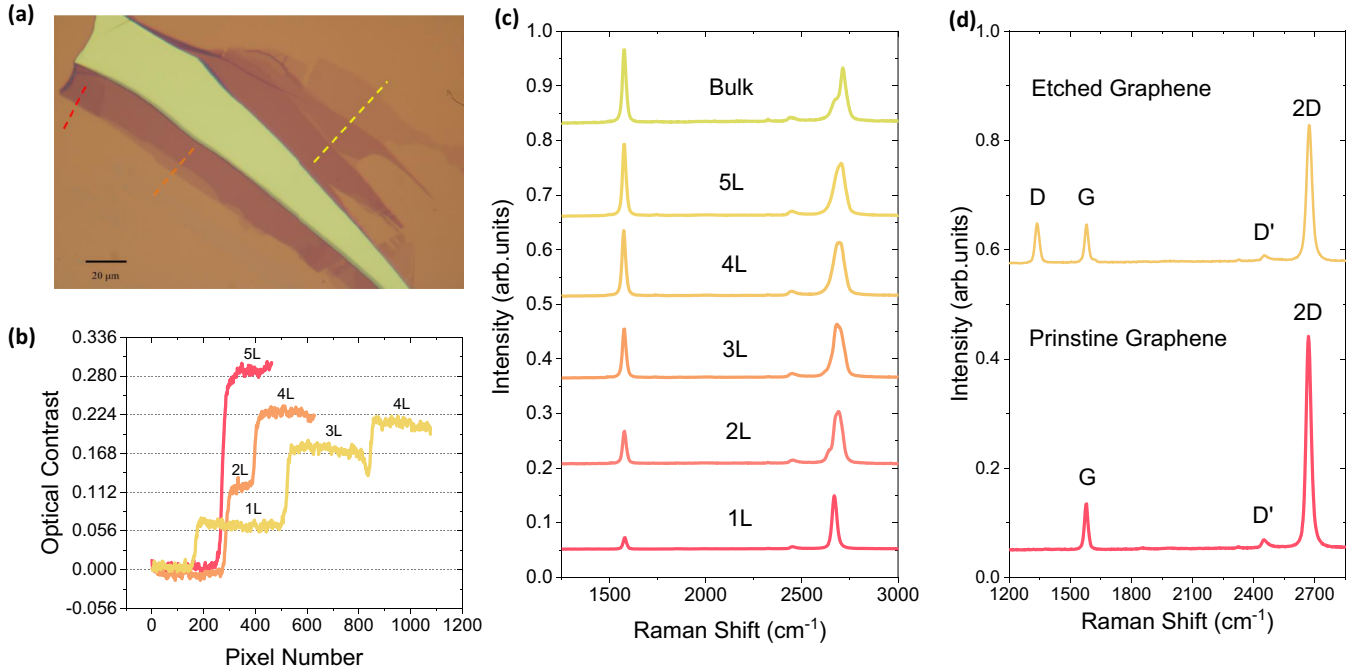

FIG. 1. (a) Optical micrograph of graphene flakes. (b) Optical contrast of graphene flakes measured along the lines in (a). (c) Unpolarized Raman spectra of few-layer (1–5 L) and thin-film (>100 L) graphite. (d) Unpolarized Raman spectra of etched monolayer graphene and pristine monolayer graphene.

graphene, we introduced defects into monolayer graphene through oxygen plasma etching (see the Methods section). The unpolarized Raman spectrum of the etched monolayer graphene exhibits prominent Raman *D* mode emission, which it is absent in pristine graphene [Fig. 1(d)] [32,33].

The helicity resolved Raman measurement was performed in a homemade optical measurement system as illustrated in Fig. S1 of the Supplemental Material [34]. The graphene flakes with different layer numbers were excited with either left ($\sigma-$) or right ($\sigma+$) circularly polarized laser and left and right circularly polarized component of Raman emissions were detected respectively (see the Methods section). We first investigated the chirality of the Raman modes in monolayer graphene at room temperature. Under $\sigma+$ excitation with photon energy of 2.33 eV, only $\sigma-$ emissions of Raman *G* mode were detected while $\sigma+$ emissions completely vanished, indicating that the Raman *G* mode perfectly switched the helicity of the incident photons [Fig. 2(a)], which is consistent with previous observation [35,36]. This perfect Raman chirality was also preserved under the excitation photon energy of 1.94 eV (Fig. S2 [34]) or $\sigma-$ excitation polarization (Fig. S3 [34]). In contrast, as shown in Figs. 2(b) and 2(c), the Raman *D* and two-dimensional (2D) modes in monolayer graphene showed no such chirality, evidenced by the insignificant difference between $\sigma+$ and $\sigma-$ component of the Raman signal under $\sigma+$ excitation.

The distinct chiral properties between graphene Raman *G*, *D*, and 2D modes can be attributed to their unique phonon scattering processes subject to the conservation of pseudoangular momentum (PAM) between graphene valleys. The Raman *G* mode arises from the intravalley scattering of excitation photons by a doubly degenerate phonon mode at the highly symmetric Brillouin zone center (Γ point) [37], where the phonon mode acquires a PAM of ±1 [38]. Since the intravalley scattering process requires the conservation of PAM, the variation of the PAM between the excitation photons and the emitting Raman photons should be equal to the PAM of the involved phonons. Therefore, the left (right) circularly polarized incident photons can only emit right- (left-) handed phonons, leading to the switching of the helicity of the Raman photons as illustrated in Fig. 2(d) [38]. On the contrary, the Raman 2D mode arises from the second order Raman process in the vicinity of the *K* and *K′* points where intervalley scattering is involved [37]. The excited electrons in the *K* valley are first scattered to the *K′* valley and then scattered back to the *K* valley by emitting a phonon in both scattering processes [Fig. 2(e)]. Since the phonons involved in these two processes have the opposite chirality, the emitted Raman photons will exhibit the same helicity as the incident photons, leading to the nonchirality of the Raman 2D mode. The Raman *D* mode involves the similar electron-phonon scattering processes to the 2D mode, while one of the scattering processes between *K* and *K′* valleys is enabled by defects instead of the phonons as illustrated in Fig. 2(e). In equilibrium, the phonon-involved scattering processes can occur either from *K* to *K′* valley or *K′* to *K* valley. Since the phonons involved in these two processes acquire the opposite PAM, the Raman *D* modes exhibit no chirality.

We then performed helicity resolved Raman spectrum measurements on pristine 2–5-L graphene and thin-film graphite (>100 L) under the excitation photon energy of 2.33 eV. The Raman 2D mode exhibits no chirality regardless of the layer number, as illustrated in Fig. 3(a). Figure 3(b) shows the polarization resolved Raman *G* mode spectra for graphene thicker than a monolayer. As illustrated in Fig. 2(a), in monolayer graphene, under $\sigma+$ excitation, the $\sigma+$ component

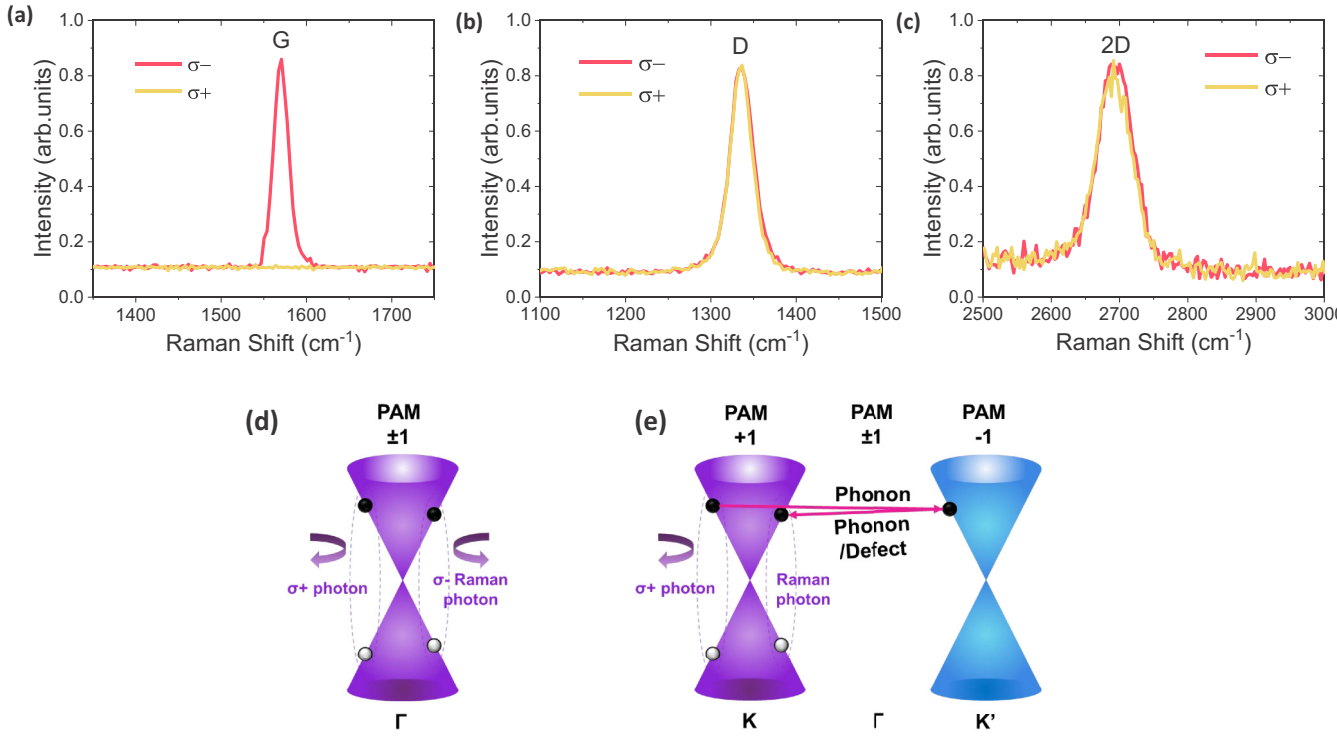

FIG. 2. Helicity resolved Raman spectra of Raman (a) *G*, (b) *D* and (c) 2D modes in monolayer graphene with excitation photon energy of 2.33 eV at room temperature. Schematic illustration of the valley phonon scattering processes and corresponding variation of PAM for Raman (d) *G*, (e) *D*, and 2D modes in monolayer graphene.

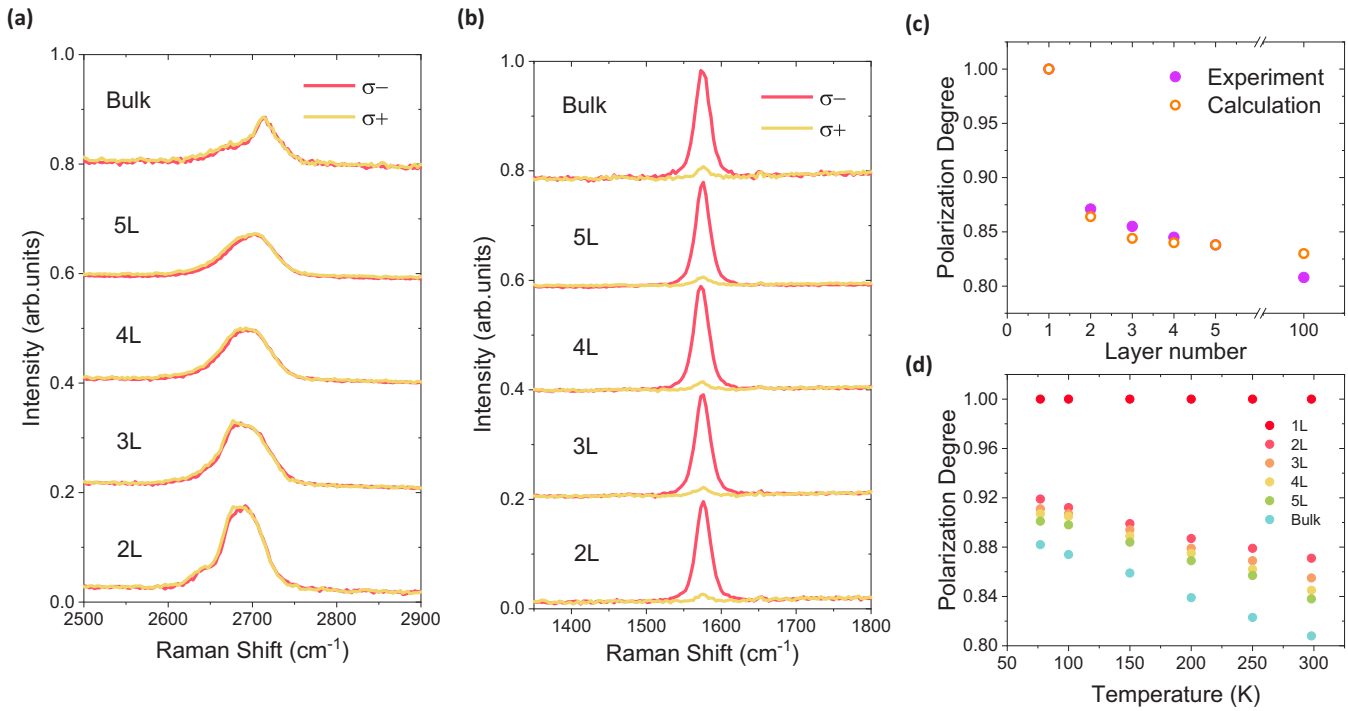

FIG. 3. Helicity resolved Raman spectra of Raman (a) 2D and (b) *G* modes in 2–5-L graphene and thin-film (>100 L) graphite with excitation photon energy of 2.33 eV at room temperature. (c) Layer number dependence of the polarization degree for graphene Raman *G* mode. (d) Temperature dependence of polarization degree for Raman *G* mode in 2–5-L graphene and thin-film graphite.

of the Raman G mode emission is completely absent. Here, a minor $\sigma+$ is observed starting from 2-L graphene and the intensity increases as graphene becomes thicker. We extracted the Raman intensities of $\sigma+$ ($I_{\min}$) and $\sigma-$ component ($I_{\max}$) respectively and calculated the polarization degree (P) of the Raman G mode using $P = (I_{\max} - I_{\min})/(I_{\max} + I_{\min})$.

In Fig. 3(c), the polarization degree (P) is plotted against the layer number of graphene, which decreases sharply from 100% in monolayer graphene to 87.1% in bilayer graphene. It further decreases monotonously and approaches its bulk limit of 80.8%, as shown in Fig. 3(c). A similar phenomenon was observed when the excitation photon energy was 1.94 eV (Fig. S4 [34]). The layer dependence of the polarization degree suggests that interlayer interaction among graphene layers significantly influences the phonon chirality.

III. ESTABLISHMENT OF RAMAN TENSORS FOR GRAPHENE LAYERS

To further understand the mechanism of the layer number dependent phonon chirality induced by interlayer interaction, we calculated the polarization degree in multilayer graphene based on symmetry analysis using Raman tensors. Here we first discuss the Raman G modes of monolayer graphene. At the Γ point, the monolayer graphene belongs to the D_{6h} point group where the Raman G mode can be described as E_{2g} representations according to the symmetry analysis, corresponding to the Raman tensor A [39], where

$$A = \begin{vmatrix} a_{11} & a_{12} & a_{11} \\ a_{21} & a_{22} & a_{23} \\ a_{31} & a_{32} & a_{33} \end{vmatrix} = \begin{vmatrix} 0 & d & 0 \\ d & 0 & 0 \\ 0 & 0 & 0 \end{vmatrix} \text{ or}$$

$$A = \begin{vmatrix} a_{11} & a_{12} & a_{11} \\ a_{21} & a_{22} & a_{23} \\ a_{31} & a_{32} & a_{33} \end{vmatrix} = \begin{vmatrix} d & 0 & 0 \\ 0 & -d & 0 \\ 0 & 0 & 0 \end{vmatrix}.$$

The left ($|\sigma_-\rangle$) and right ($|\sigma_+\rangle$) circularly polarized wave vectors are defined as

$$|\sigma_-\rangle = \frac{1}{\sqrt{2}}(1 \quad i \quad 0)^T \quad \text{and}$$

$$|\sigma_+\rangle = \frac{1}{\sqrt{2}}(1 \quad -i \quad 0)^T, \quad \text{respectively.}$$

The normalized Raman intensity for different excitation/detection configuration can be calculated as $|\sigma_i^\dagger A \sigma_j|^2$, where both i and j can be "−" or "+." For excitation/detection configuration with the same polarization ($i = j$), the Raman signal completely vanishes as $I_{\min} = |\sigma_i^\dagger A \sigma_j|^2 = 0$. In contrast, for an excitation/detection configuration with the opposite polarization where $i \neq j$, the Raman intensity reaches its maximum as $I_{\max} = |\sigma_i^\dagger A \sigma_j|^2 = d^2$.

Furthermore, we established the Raman tensor for the Raman G mode in bilayer graphene by adding an additional interlayer hopping term [40,41], which can be represented by a 6×6 matrix R,

$$R = \begin{vmatrix} A & B \\ B & A \end{vmatrix}.$$

Here the A matrix is the same as that in monolayer graphene and B is the matrix representation of the interlayer coupling term, which is defined as

$$B = \begin{vmatrix} t_{11} & t_{12} & t_{13} \\ t_{21} & t_{22} & t_{23} \\ t_{31} & t_{32} & t_{33} \end{vmatrix}.$$

The matrix element t_{ij} ($i,\ j = 1,\ 2,\ 3$) is defined as the interlayer coupling coefficient between the adjacent graphene layers where $t_{ji} = t_{ij}$ due to the symmetry. The left and right circularly polarized wave vectors are also extended to be compatible with the Raman tensor, which are defined as

$$|\sigma_-\rangle = \frac{1}{\sqrt{2}}(1 \quad i \quad 0 \quad 1 \quad i \quad 0)^T \quad \text{and}$$

$$|\sigma_+\rangle = \frac{1}{\sqrt{2}}(1 \quad -i \quad 0 \quad 1 \quad -i \quad 0)^T, \quad \text{respectively.}$$

Similarly, $|\sigma_i^\dagger A \sigma_j|$ is used to calculate the Raman intensity under the different excitation/detection polarization configurations. For an excitation/detection configuration with the same polarization, the Raman intensity is

$$I_{\min} = |\sigma_+^\dagger A \sigma_+|^2 = |\sigma_-^\dagger A \sigma_-|^2 = (t_{11} + t_{22})^2,$$

which is nonvanishing in contrast to that in monolayer graphene. While for an excitation/detection configuration with the opposite polarization, the Raman intensity is

$$I_{\max} = |\sigma_+^\dagger A \sigma_-|^2 = |\sigma_-^\dagger A \sigma_+|^2 \approx 4d^2.$$

Therefore the polarization degree of the Raman G mode in bilayer graphene is

$$P_2 = \frac{I_{\max} - I_{\min}}{I_{\max} + I_{\min}} = \frac{4d^2 - (t_{11} + t_{22})^2}{4d^2 + (t_{11} + t_{22})^2}.$$

According to the Raman tensor calculation, the polarization degree in bilayer graphene will not be perfect (100%) due to the existence of the interlayer interaction coefficient. However, since the interlayer coupling coefficient t_{ij} should be significantly smaller than the fundamental Raman tensor term d, the polarization degree will not decrease significantly, evidenced by the low intensity Raman signal under an excitation/detection configuration with the same polarization. The polarization degree of the Raman G mode in trilayer and multilayer graphene were calculated accordingly, where

$$P_3 = \frac{I_{\max} - I_{\min}}{I_{\max} + I_{\min}} = \frac{4d^2 - (t_{11} + t_{22} + t_{44} + t_{55})^2}{4d^2 + (t_{11} + t_{22} + t_{44} + t_{55})^2},$$

$$P_n = \frac{I_{\max} - I_{\min}}{I_{\max} + I_{\min}} = \frac{4d^2 - (t_{11} + t_{22} + t_{44} + t_{55} + t_{77} + t_{88} + \cdots + t_{3n-5,3n-5} + t_{3n-4,3n-4})^2}{4d^2 + (t_{11} + t_{22} + t_{44} + t_{55} + t_{77} + t_{88} + \cdots + t_{3n-5,3n-5} + t_{3n-4,3n-4})^2}.$$

The detailed calculation process was provided in Supplemental Material Sec. VI [34]. Here, t_{3n-5} and t_{3n-4} represents the interlayer coupling coefficient between the adjacent n layers, which decays significantly with the increasing n. Therefore, in multilayer graphene, the polarization degree of the Raman G mode will decrease with increasing layer numbers, which is consistent with our measurements.

To further verify the established model, we calculated the polarization degree by deducting the value of interlayer coupling coefficient t_{ii}. The value of the $(t_{11}+t_{22})^2$ was directly extracted from the helicity resolved Raman spectrum in bilayer graphene, which exhibits a polarization degree of 87.1%. Therefore, the value of interlayer coupling coefficient in the adjacent graphene layers was determined as $(t_{11}+t_{22})^2 = 0.3d^2$. Since we assume that the interlayer interaction in graphene layers is contributed by dipole-dipole interaction which decays with the distance by $1/r^3$ [42], the interlayer coupling coefficient in adjacent three layers can be estimated as

$$(t_{44}+t_{55})^2 = \tfrac{1}{8}(t_{11}+t_{22})^2 = 0.0375d^2.$$

Therefore the calculated polarization degree of the Raman G mode in trilayer graphene is 84.4%, which agrees well with our experimental result (85.5%). Similarly, we can further deduct the interlayer coupling coefficient in adjacent n layers, which gives

$$(t_{3n-5,3n-5}+t_{3n-4,3n-4})^2 = \frac{1}{(n-1)^3}(t_{11}+t_{22})^2.$$

Then when n is very large, we have

$$(t_{11}+t_{22}+t_{44}+t_{55}+t_{44}+t_{55}+\cdots + t_{3n-5,3n-5}+t_{3n-4,3n-4})^2 = 0.36d^2.$$

Therefore the calculated polarization degree of the Raman G mode in thin-film graphite should be 83.0%, which also agrees well with the experimental results (80.8%). The evolution of the polarization degree against the layer number from Raman tensor calculation is also plotted in Fig. 3(c) together with the experimental results. It is clear that our model captures the impact of interlayer coupling on the phonon chirality.

IV. TEMPERATURE DEPENDENCE OF THE PHONON CHIRALITY

We further investigated the temperature dependence of the polarization degree in graphene Raman G mode. In monolayer graphene, the perfect phonon chirality was preserved at all temperatures, as illustrated in Fig. 3(d). Moreover, Fig. 3(d) also shows the degree of polarization as a function of the temperature for multilayer graphene. In general, the degree of polarization decreases as the temperature increases. The temperature dependence of the polarization degree indicates the role of interlayer phonon-phonon interaction, which suppresses the degree of phonon polarization. Reduced temperature can freeze the lattice vibration and therefore suppress the interlayer phonon-phonon interaction in multilayer graphene and facilitates the preservation of the phonon chirality. We applied the same model to simulate the evolution of the polarization degree against the layer number at 77 K (see Supplemental Material Sec. VII [34]). The calculated polarization degree also agrees with the experimental results well (Fig. S5 [34]).

V. HELICITY RESOLVED RAMAN SPECTRUM IN hBN LAYERS

In addition, we performed helicity resolved Raman measurements on another 2D honeycomb material, hexagonal boron nitride (hBN). Monolayer hBN on SiO_2/Si substrate was transferred from hBN on copper grown by chemical vapor deposition (see the Methods section). We also prepared thin-film hBN (>100L) by mechanical exfoliation from bulk crystal. Figure 4(a) shows the unpolarized Raman E_{2g} mode measurements. The Raman E_{2g} mode peaks at 1368.5 and 1366 cm^{-1} for monolayer and bulk hBN, respectively, consistent with previous reports [43,44]. We then performed the helicity resolved Raman measurements in both monolayer and thin-film hBN under 2.33-eV $\sigma+$ excitation at room temperature. The perfect phonon chirality was only preserved in monolayer hBN as shown by the top panel of Fig. 4(b). For thin-film hBN, a clear $\sigma+$ peak was observed [lower panel of Fig. 4(b)]. The temperature dependence of the polarization degree in hBN Raman E_{2g} modes for both monolayer and thin-film hBN is plotted in Fig. 4(c). The phonon chirality remains perfect at all temperatures in monolayer hBN, while the degree of polarization decreases at elevated temperature in thin-film hBN. The layer number and temperature dependent chiral Raman modes in hBN further illustrate the role of the interlayer phonon-phonon interactions, which can affect the lattice vibration in 2D honeycomb lattice.

VI. DISCUSSION

Previously, the circular polarization of the Raman emission has also been investigated in monolayer and few-layer transitional metal dichalcogenides (TMDs) [39]. The Raman emission due to out-of-plane relative motion of only chalcogen atoms (OC) mode has the same polarization state of the excitation photons. In contrast, the Raman emission due to in-plane relative motion of transition metal and chalcogen atoms (IMC) mode exhibits opposite circular polarization if compared with the circular polarization of the excitation photons. Remarkably, the circular polarization of Raman emission due to the OC modes remains perfect regardless of the layer number, while it becomes imperfect for Raman emission due to the IMC modes in multilayers. This observation suggests that the in-plane vibration modes are less robust to interlayer interactions compared with the out-of-plane vibration modes in TMDs. In graphene and hBN, the Raman active G mode is only contributed by the in-plane lattice vibrations, while the out-of-plane lattice vibration modes are Raman inactive [44,45]. Although it is not feasible to investigate the impact of interlayer coupling on out-of-plane modes in graphene and hBN using Raman scattering, our observation of the imperfect and layer-dependent phonon chirality of the Raman G mode is consistent with the previously reported results on the IMC modes in TMDs [39].

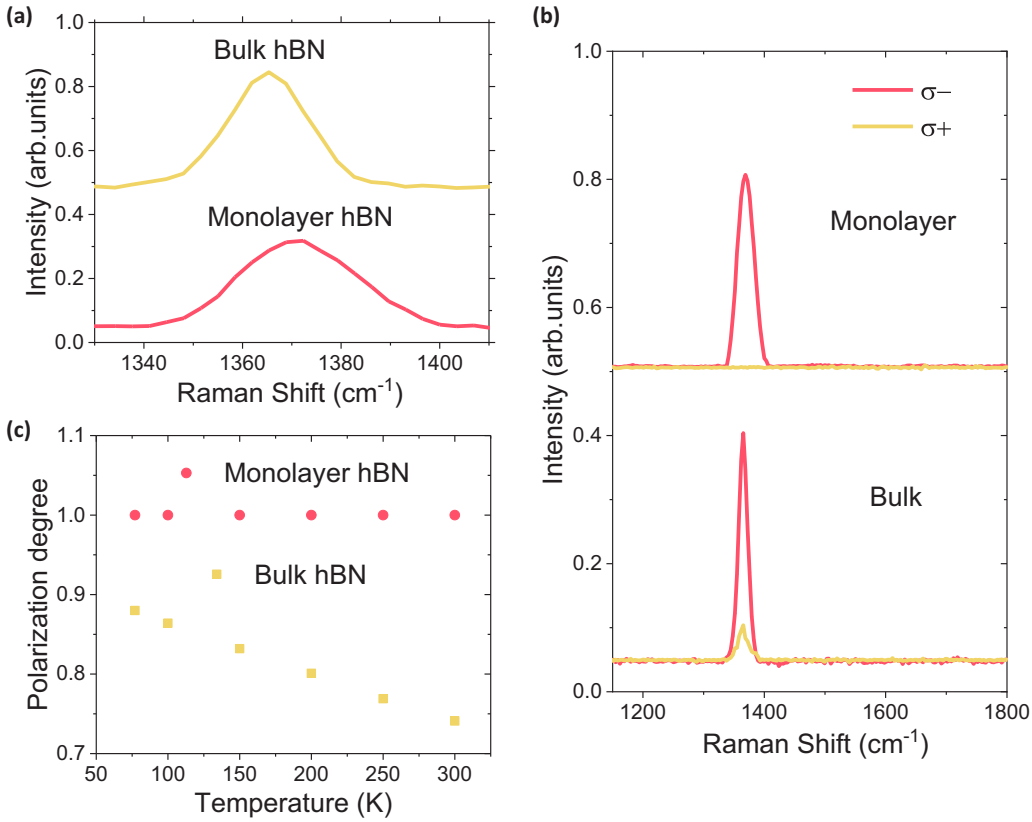

FIG. 4. (a) Unpolarized Raman spectra of monolayer and bulk hBN. (b) Helicity resolved Raman spectra of monolayer and bulk hBN with excitation photon energy of 2.33 eV at room temperature. (c) Temperature dependence of polarization degree for Raman *G* mode in monolayer and bulk hBN.

VII. CONCLUSION

In conclusion, here we report a comprehensive investigation on the vdW interlayer interactions in honeycomb lattice via chiral phonons. The interlayer interaction plays an important role in lattice vibrations of the honeycomb lattice and therefore affects the phonon chirality, evidenced by the decreasing polarization degree of Raman *G* modes with increasing layer number and temperature. We further established a method to construct the tensor for Raman *G* modes in multilayer 2D honeycomb lattice by introducing the interlayer coupling coefficients, which characterizes the strength of the interlayer interaction. The layer dependent phonon chirality extracted from Raman tensor calculation agrees with the helicity resolved Raman measurement results well. Our observations provide a different perspective to probe the interlayer interaction in vdW materials and heterostructures with unique honeycomb lattice symmetry.

VIII. METHODS

A. Sample preparation

Monolayer and few-layer graphene flakes were mechanically exfoliated to the 90-nm SiO_2/Si substrate and then were identified under an optical microscope. The Raman *D* peak in graphene was introduced through gentle oxygen plasma (plasma power: 10 W; oxygen flow: 10 sccm; duration: 1 s). Large area chemical vapor deposition monolayer hBN on copper (2 × 2 inches) was purchased from HQ graphene. First, a 400-nm-thick PMMA layer was spin-coated onto the hBN/copper surface. Second, the PMMA/hBN/copper was floated on the $FeCl_3$ solvent with copper layer downside for 30 min to etch off the copper substrate. Then the PMMA/hBN layer was washed with DI water and was picked up by the 90 nm SiO_2/Si substrate. Finally, the PMMA layer was washed out by acetone.

B. Optical measurements

The helicity resolved Raman measurements were performed in a micro-optical measurement system as shown in Fig. S1 [34]. A combination of a linear polarizer and a broadband quarter-wave plate was used to generate the left/right circularly polarized excitation, which was focused onto the sample by a 40× microscope objective. The backscattered Raman signal was first depolarized by the same quarter-wave plate, then the left/right circularly polarized component of the signal was analyzed by a combination of broadband half-wave plate and a linear polarizer. The Raman signal was further collected and analyzed by an Andor Sharmock SR750 spectrometer equipped with an iDus 420 series charge-coupled device camera. The sample was mounted in Janis ST-500 microscopy cryostat for both room temperature and low temperature measurements. Two continuous solid-state lasers with excitation photon energies of 1.90 and 2.33 eV were used as the excitation sources.

ACKNOWLEDGMENTS

We acknowledge the partial financial support from the National Science Foundation (NSF) EFRI-NewLAW program (Grant No. 1741693). K.W. and T.T. acknowledge support from the Elemental Strategy Initiative conducted by the MEXT, Japan (Grant No. JPMXP0112101001), JSPS KAKENHI (Grant No. JP20H00354), and CREST (Grant No. JPMJCR15F3), JST. S.H. acknowledges support from the National Science Foundation under Grant No. ECCS-1943895.

[1] P. Ajayan, P. Kim, and K. Banerjee, Phys. Today **6(9)**, 38 (2016).

[2] K. S. Burch, D. Mandrus, and J.-G. Park, Nature (London) **563**, 47 (2018).

[3] D. N. Basov, M. M. Fogler, and F. J. García de Abajo, Science **354**, aag1992 (2016).

[4] J. R. Schaibley, H. Yu, G. Clark, P. Rivera, J. S. Ross, K. L. Seyler, W. Yao, and X. Xu, Nat. Rev. Mater. **1**, 16055 (2016).

[5] J. Wang, S. Deng, Z. Liu, and Z. Liu, Natl. Sci. Rev. **2**, 22 (2015).

[6] C.-h. Liu, J. Zheng, Y. Chen, T. Fryett, and A. Majumdar, Opt. Mater. Express **9**, 384 (2019).

[7] D. Jariwala, A. R. Davoyan, J. Wong, and H. A. Atwater, ACS Photonics **4**, 2962 (2017).

[8] G. Fiori, F. Bonaccorso, G. Iannaccone, T. Palacios, D. Neumaier, A. Seabaugh, S. K. Banerjee, and L. Colombo, Nat. Nanotechnol. **9**, 768 (2014).

[9] F. H. L. Koppens, T. Mueller, P. Avouris, A. C. Ferrari, M. S. Vitiello, and M. Polini, Nat. Nanotechnol. **9**, 780 (2014).

[10] T. Cheiwchanchamnangij and W. R. L. Lambrecht, Phys. Rev. B **85**, 205302 (2012).

[11] A. Splendiani, L. Sun, Y. Zhang, T. Li, J. Kim, C.-Y. Chim, G. Galli, and F. Wang, Nano Lett. **10**, 1271 (2010).

[12] V. Tran, R. Soklaski, Y. Liang, and L. Yang, Phys. Rev. B **89**, 235319 (2014).

[13] G. Zhang, S. Huang, A. Chaves, C. Song, V. O. Özçelik, T. Low, and H. Yan, Nat. Commun. **8**, 14071 (2017).

[14] L. Li, J. Kim, C. Jin, G. J. Ye, D. Y. Qiu, F. H. da Jornada, Z. Shi, L. Chen, Z. Zhang, F. Yang *et al.*, Nat. Nanotechnol. **12**, 21 (2017).

[15] C. Chen, F. Chen, X. Chen, B. Deng, B. Eng, D. Jung, Q. Guo, S. Yuan, K. Watanabe, T. Taniguchi *et al.*, Nano Lett. **19**, 1488 (2019).

[16] X. Wang, A. M. Jones, K. L. Seyler, V. Tran, Y. Jia, H. Zhao, H. Wang, L. Yang, X. Xu, and F. Xia, Nat. Nanotechnol. **10**, 517 (2015).

[17] T. Björkman, A. Gulans, A. V. Krasheninnikov, and R. M. Nieminen, Phys. Rev. Lett. **108**, 235502 (2012).

[18] E. Mostaani, N. D. Drummond, and V. I. Fal'ko, Phys. Rev. Lett. **115**, 115501 (2015).

[19] L. Spanu, S. Sorella, and G. Galli, Phys. Rev. Lett. **103**, 196401 (2009).

[20] J. M. Gonzalez and I. I. Oleynik, Phys. Rev. B **94**, 125443 (2016).

[21] A. Klein, S. Tiefenbacher, V. Eyert, C. Pettenkofer, and W. Jaegermann, Phys. Rev. B **64**, 205416 (2001).

[22] G. Constantinescu, A. Kuc, and T. Heine, Phys. Rev. Lett. **111**, 036104 (2013).

[23] X. Luo, X. Lu, G. K. W. Koon, A. H. Castro Neto, B. Özyilmaz, Q. Xiong, and S. Y. Quek, Nano Lett. **15**, 3931 (2015).

[24] Y. Zhao, X. Luo, H. Li, J. Zhang, P. T. Araujo, C. K. Gan, J. Wu, H. Zhang, S. Y. Quek, M. S. Dresselhaus *et al.*, Nano Lett. **13**, 1007 (2013).

[25] Y. Zhao, J. Qiao, P. Yu, Z. Hu, Z. Lin, S. P. Lau, Z. Liu, W. Ji, and Y. Chai, Adv. Mater. **28**, 2399 (2016).

[26] Z. Wu, Y. Han, J. Lin, W. Zhu, M. He, S. Xu, X. Chen, H. Lu, W. Ye, T. Han *et al.*, Phys. Rev. B **92**, 075408 (2015).

[27] F. Parhizgar, A. Qaiumzadeh, and R. Asgari, Phys. Rev. B **96**, 075447 (2017).

[28] M. Bayle, N. Reckinger, A. Felten, P. Landois, O. Lancry, B. Dutertre, J.-F. Colomer, A.-A. Zahab, L. Henrard, J.-L. Sauvajol *et al.*, J. Raman Spectrosc. **49**, 36 (2018).

[29] X.-L. Li, W.-P. Han, J.-B. Wu, X.-F. Qiao, J. Zhang, and P.-H. Tan, Adv. Funct. Mater. **27**, 1604468 (2017).

[30] Y. Hao, Y. Wang, L. Wang, Z. Ni, Z. Wang, R. Wang, C. K. Koo, Z. Shen, and J. T. L. Thong, Small **6**, 195 (2010).

[31] Z. Ni, Y. Wang, T. Yu, and Z. Shen, Nano Res. **1**, 273 (2008).

[32] A. Eckmann, A. Felten, A. Mishchenko, L. Britnell, R. Krupke, K. S. Novoselov, and C. Casiraghi, Nano Lett. **12**, 3925 (2012).

[33] E. H. Martins Ferreira, M. V. O. Moutinho, F. Stavale, M. M. Lucchese, R. B. Capaz, C. A. Achete, and A. Jorio, Phys. Rev. B **82**, 125429 (2010).

[34] See Supplemental Material at http://link.aps.org/supplemental/10.1103/PhysRevB.103.035405 for additional experimental evidence.

[35] S. G. Drapcho, J. Kim, X. Hong, C. Jin, S. Shi, S. Tongay, J. Wu, and F. Wang, Phys. Rev. B **95**, 165417 (2017).

[36] Y. Tatsumi and R. Saito, Phys. Rev. B **97**, 115407 (2018).

[37] L. M. Malard, M. A. Pimenta, G. Dresselhaus, and M. S. Dresselhaus, Phys. Rep. **473**, 51 (2009).

[38] L. Zhang and Q. Niu, Phys. Rev. Lett. **115**, 115502 (2015).

[39] S.-Y. Chen, C. Zheng, M. S. Fuhrer, and J. Yan, Nano Lett. **15**, 2526 (2015).

[40] M. Koshino, Phys. Rev. B **81**, 125304 (2010).

[41] F. Zhang, B. Sahu, H. Min, and A. H. MacDonald, Phys. Rev. B **82**, 035409 (2010).

[42] N. W. Ashcroft and N. D. Mermin, *Solid State Physics* (Cengage Learning, New York, 2011).

[43] T. T. Tran, K. Bray, M. J. Ford, M. Toth, and I. Aharonovich, Nat. Nanotechnol. **11**, 37 (2016).

[44] R. V. Gorbachev, I. Riaz, R. R. Nair, R. Jalil, L. Britnell, B. D. Belle, E. W. Hill, K. S. Novoselov, K. Watanabe, T. Taniguchi *et al.*, Small **7**, 465 (2011).

[45] A. C. Ferrari and D. M. Basko, Nat. Nanotechnol. **8**, 235 (2013).